Towards advanced Geological Mapping of Precambrian Rocks in the El Ineigi Area, Central Eastern Desert, Egypt: Integrating Hyperspectral Satellite Data and Machine Learning algorithm

Ahmed M. Abdelhameed[1,2*], Maher El Amawy[3], Ayman Mahrous[1,4], Mohamed E. El-Khouly[5], and Adel Fathy[1,6]

1. Department of Space Environment, Institute of Basic and Applied Sciences, Egypt-Japan University of Science and Technology (E-JUST), New Borg El-Arab City, Alexandria 21934, Egypt
2. Geology Department, Faculty of Science, Sohag University, Sohag 82524, Egypt
3. Department of Geology, Faculty of Science, Benha University, Benha 13518, Egypt
4. Department of Physics, Faculty of Science, Helwan University, Helwan, Cairo 11795, Egypt
5. Nanoscience Program, Institute of Basic and Applied Science, Egypt-Japan University of Science and Technology (E-JUST), New Borg El-Arab City, Alexandria 21934, Egypt
6. Physics Department, Faculty of Science, Fayoum University, Fayoum 63514, Egypt

Article Info

Abstract

Hyperspectral imaging (HSI), combined with advanced machine learning algorithms (MLAs), has unlocked novel research opportunities and revolutionized geological mapping by enabling precise lithological classification. Accurately detailed geological mapping is one of the most essential requirements for targeting mineralization. However, achieving comprehensive lithological mapping remains a challenge, hindering systematic mineral exploration. This work explores the use of PRISMA hyperspectral data and the Support Vector Machine (SVM) and Artificial Neural Network (ANN) algorithms to objectively map the Precambrian rock assemblages at the El Ineigi area in the Central Eastern Desert (CED) of Egypt. For this purpose, PRISMA data in HDF5 format were first pre-processed and subsequently transformed through principal component analysis (PCA). The processed spectral data were then combined with extensive fieldwork and previously existing geological maps and classified using SVM and ANN to achieve enhanced discrimination of the exposed rock units in the study area. Our results conclusively demonstrate the exceptional capability of PRISMA data for detailed lithological mapping. The SVM and ANN classification achieved remarkably high overall accuracy, successfully generating a robust geological map that clearly discriminates between various Neoproterozoic basement rock units in the El Ineigi area. Through the integration of diagnostic spectral signatures with field verification, we confidently identified all major mappable units, including metavolcanics, metagabbro-diorite complexes, younger granites, and Wadi deposits. The proposed integrated approach demonstrates superior performance compared to traditional mapping techniques, offering enhanced discrimination precision and operational efficiency. These findings strongly support the combined use of PRISMA hyperspectral data and MLAs for lithological mapping applications.

1. Introduction

Accurate understanding of the lithological composition of the Earth's surface is crucial for various domains, including mineral exploration [1, 2], natural resource management [3-5], land-use planning [6], and geological hazard assessment [7]. Lithological maps offer valuable information regarding crustal composition, the spatial distribution of rock units, and the regional geological evolution. Traditionally, lithological classification relied on time-consuming and costly

field surveys, which were often limited by restricted spatial coverage [8, 9]. The rise of remote sensing technologies in the 1960s marked a transformative shift, providing a faster and more cost-effective approach to data acquisition and interpretation, offering a more efficient alternative to conventional techniques [10], particularly advantageous in arid and semi-arid regions with optimal surface exposure [11].

Several remote sensing datasets, including multispectral data sets such as ASTER (Advanced Spaceborne Thermal Emission and Reflection Radiometer), Sentinel, and Landsat satellite imagery, have been widely employed for lithological mapping, producing satisfactory outcomes. However, the limited number of spectral bands of the multispectral sensors, especially in the shortwave infrared (SWIR) region, restricts their capacity to resolve complex mineralogical variations. Hyperspectral remote sensing technologies, such as PRISMA (PRecursore IperSpettrale della Missione Applicativa), EnMAP (Environmental Mapping and Analysis Program), and HISUI (Hyperspectral Imager Suite), offer significant advantages. These sensors capture hundreds of narrow, contiguous spectral bands across the visible to shortwave infrared spectrum (0.4–2.5 μm). The enhanced spectral detail of hyperspectral images (HSIs) allows for the precise characterization of rock units and compositional variations, significantly improving geological interpretation and therefore enabling detailed mineralogical and lithological discrimination [12-14]. Among these, PRISMA is particularly notable for its high spectral resolution (234 bands) and open-access availability. It has recently proven effective in lithological mapping across various regions, including the Arabian-Nubian Shield (ANS) [13, 15, 16].

Simultaneously, advancements in computer technology and artificial intelligence (AI) have introduced machine learning (ML) techniques as powerful tools for remote sensing data analysis. ML methods, particularly supervised learning algorithms, can model complex relationships between input features and target classifications, enhancing both accuracy and computational efficiency [17]. MLAs encompass a diverse range of algorithms, broadly categorized into supervised and unsupervised learning methods. Supervised learning algorithms employ sophisticated statistical and non-probabilistic approaches to identify patterns within geological datasets. Moreover, models are trained using labeled datasets, where each input corresponds to a known

output [18]. These algorithms optimize model parameters to maximize accuracy while mitigating overfitting [19].

Among supervised ML algorithms, Support Vector Machines (SVM) and Artificial Neural Networks (ANNs) have shown particular promise. SVM has gained popularity in lithological and mineral prospectivity mapping due to its robustness and ability to construct nonlinear decision boundaries in high-dimensional spaces, outperforming traditional classification methods like the Spectral Angle Mapper (SAM) [20–22]. Numerous recent studies have validated its effectiveness in geological applications [23–33]. Similarly, ANNs also have gained significant recognition within geoscience applications [34, 35]. ANNs have demonstrated strong performance in lithological classification [28, 36-39], attributable to their adaptability, ability to model nonlinear relationships, and capacity to incorporate spatial context [40]. Complementing these machine learning approaches, Principal Component Analysis (PCA) is frequently employed to further enhance classification performance by transforming high-dimensional datasets into a lower-dimensional space while preserving key spectral features, thereby increasing algorithmic efficiency and reducing noise, which is particularly valuable in geologically complex terrains [22, 24, 28, 41].

Building on the demonstrated effectiveness of hyperspectral remote sensing and ML in lithological mapping, the current study introduces a robust classification framework for detailed lithological mapping of the El Ineigi area. This region, located in the southern part of the Central Eastern Desert (CED) of Egypt, lies approximately 75 km northwest of Mersa Alam along the road to Idfu, bounded by latitudes 25° 11' and 25° 15' N and longitudes 34° 04' and 34° 10' E and covering an area of about 70 km² (Figure 1A and 1B). This study utilizes PRISMA hyperspectral data in conjunction with a comparative evaluation of SVM and ANN classifiers to enhance lithological discrimination of Precambrian basement rocks. The motivation for this work stems from the outdated and inconsistent nature of the existing geological maps of the study area, last updated in 2008 [43] (Figure 1C), which contain significant discrepancies due to subjective interpretation inherent in conventional field-based mapping approaches and limited data integration. The current work comes with a clear objective of generating a more accurate, objective, and up-to-

date geological map of the El Ineigi area by integrating high-resolution hyperspectral imagery with advanced ML algorithms for the first time in this region, aiming to take part in addressing the critical gaps in current geological knowledge and detailed maps of the study area. The classification results are rigorously validated through detailed fieldwork and petrographic analysis, ensuring the scientific robustness and practical relevance of the study. Finally, the outcomes of this work contribute to filling existing knowledge gaps and addressing the shortcomings of earlier maps. The resulting map not only resolves previous inconsistencies but also serves as a valuable tool for guiding mineral exploration and resource assessment efforts in the study area.

(a) Simplified geologic map of Eypt, (after [42]).

(b) Satellite image of the study area created by ArcGIS Desktop v 10.8.

(c) Geologic map of the El Ineigi area, sourced from the previous work [43].

Figure 1. Location and geologic maps of the study area.

2. General Geology

Detailed field investigations of the El Ineigi area revealed the following key geological features:

i) The El-Ineigi area is predominantly occupied by Precambrian crystalline rocks, including island arc metavolcanics (Figure 2A), metagabbro-diorite complex (Figure 2B), and post-orogenic granitic suite that is primarily represented by

3

highly fractionated alkali-feldspar granite (AFG) beside wadi deposits. The AFG rocks form massive, medium- to coarse-grained intrusions with a distinctive pink to light pink coloration. They are partially albitized and frequently occur as conformable slices hanging over each other (Figure 2C). These granites intruded pre-existing rocks, such as the metagabbro-diorite complex. Distinct, sharp contacts are observable between the granitic body and adjacent metagabbros (exposed along the northern and western margins) (Figure 2D), with no observable evidences of thermal alteration. Furthermore, the El-Ineigi granites are entirely devoid of xenoliths derived from the surrounding country rocks. Additionally, the granitoid pluton forms the most prominent topographic feature in the eastern and northern sectors of the study area, reflecting their relatively younger emplacement age and more resistant nature. ii) The investigated Neoproterozoic rock units are intensely fractured, with dominant joint systems oriented along NW-SE and NE-SW trends (Figure 2E). These fracture patterns are consistent with regional fault trends in the region [43], suggesting structural control on the emplacement and deformation fabric of the pluton. iii) Extensive quartz and fluorite-quartz vein systems (Figure 2F) are predominantly concentrated in the northern and central sectors of the pluton. These display white to greenish-white colors and range in thickness from 0.5 to 4.0 meters. The general trend of these veins is NW-SE directions. However, less common pure fluorite veins also crosscut the granitic body, which is also observed, and they have limited surface outcrops. In the southern and western portions of the pluton, such fluorite veins are often obscured by granitic colluvial deposits reaching several meters in thickness [43].

3. Materials and methods

In the current study, the methodology follows a series of meticulously designed stages for processing data from multiple sources. Each step is aimed at maximizing the accuracy and reliability of the analysis, enabling a comprehensive understanding of the lithological features within the study area. The methods used in this analysis are outlined in the flowchart of Figure 3. Data processing and analysis were conducted using Environment for Visualizing Images (ENVI) version 5.6 and ArcGIS 10.8.

3.1. Remote sensing datasets description

The PRISMA hyperspectral imaging system, launched in March 2019 by the Italian Space Agency (ASI), represents a significant advancement in spaceborne hyperspectral remote sensing. The sensor's exceptional capabilities include 234 contiguous spectral channels covering the Visible-Near Infrared (VNIR) to Short-Wave Infrared (SWIR) within a wavelength range of 0.4-2.5 μm with a spectral resolution of ~ 12 nm [15, 44, 45]. PRISMA acquires data at 30 m spatial resolution for hyperspectral bands and 5 m for the panchromatic channel, with a 30 km swath width from its sun-synchronous orbit at 614.8 km altitude and 97.751° inclination. According to their utility, PRISMA products are divided and subdivided into Level 0, which contains raw binary data including ancillary information; Level 1, which comprises radiometrically and geometrically calibrated hyperspectral cubes and panchromatic radiance images; and Level 2 processing, which is in charge of transforming the L1 Top-of-Atmosphere (TOA) spectral radiance into geophysical parameters (L2B, L2C, and L2D). Images of geolocated on-ground radiance (L2B), geolocated reflectance (L2C), and geolocated and geocoded on-ground reflectance images (L2D) are provided [46]. The mission provides free data access to registered users after validation, including both archived and newly acquired scenes. For the current study, a cloud-free surface reflectance PRISMA hyperspectral scene of the study area (PRS_L2D_STD_20250127083216_2025012708 3221_0001) was acquired and downloaded from the official portal (https://PRISMA.asi.it) on March 8, 2025.

3.2. Hyperspectral Data Preprocessing

In this stage, the dataset underwent layer stacking to combine multiple spectral bands into a single cohesive image. Subsequently, the stacked data were subset to focus on the study area boundaries, ensuring spatial consistency. Additionally, complementary lithological maps were carefully analyzed alongside the PRISMA hyperspectral data to facilitate a more accurate and detailed geological interpretation of the exposed rock units within the study area.

(a) Highly sheared metavolcanics (Mvs) and wadi deposits (WD)

(b) General view of highly sheared metagabbro-diorite complex (MGD) and WD

(c) Younger granites (YGr) dipping E and coming up ward as slices hanging over each other

(d) Intrusive contact of YGr with MGD

(e) Pervasive foliation in highly foliated MGD

(f) Close up view showing large fluorite crystals within quartz vein.

Figure 2. Field photographs

3.3. Spectral signatures of lithologies:

Spectral signature analysis is a profile representing the reflectance and thermal response of individual pixels across multiple spectral bands. The spectral signature of a rock unit depends on the intrinsic spectral properties of its chemical constituents and the molecular structure of its minerals. Given the complexity of hyperspectral data and the intricate spectral signatures of different lithological units, spectral signature profiles were applied to characterize each rock unit exposed within the study area. This approach enabled the assessment of how these rock units reflect light over the various PRISMA hyperspectral bands.

5
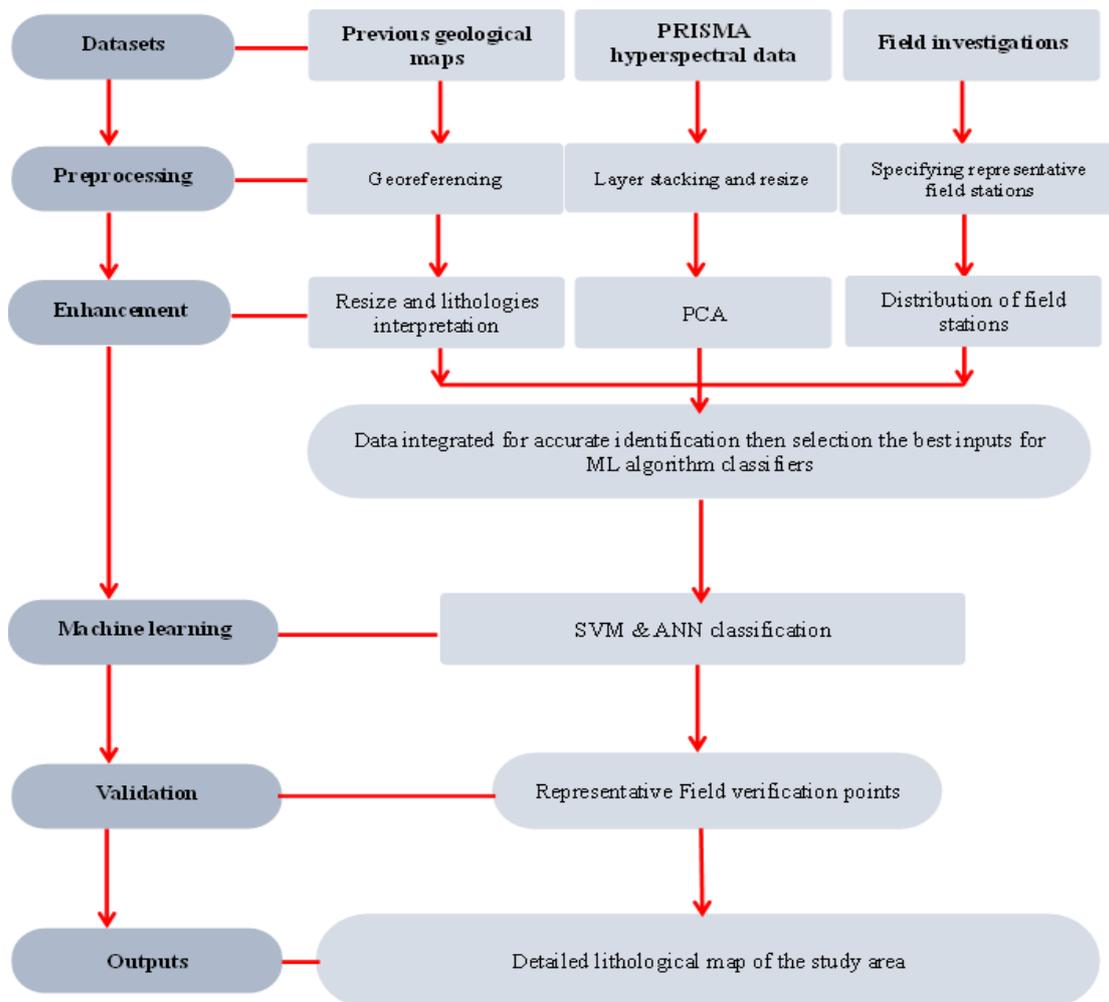
Figure 3. Flow chart showing the methodology adopted in the current study.

Spectral reflectance profiles were derived from the PRISMA hyperspectral imagery, specifically utilizing the Visible and Near-Infrared (VNIR) and Shortwave Infrared (SWIR) bands. For each of the four dominant rock units, 40 randomly selected regions of interest (ROIs), each measuring 10 × 10 pixels, were sampled. The average reflectance spectra were calculated from these ROIs to generate representative spectral curves (Figure 4A and 4B). These spectral signatures allow for precise differentiation of various rock units by highlighting their unique spectral behaviors and supporting the interpretation of their mineralogical characteristics.

The general spectral trends observed across the four lithological units (Figure 4A) revealed distinct reflectance patterns across PRISMA's VNIR and SWIR bands. Wadi deposits exhibited the highest overall reflectance (digital number), followed by granite, which displayed moderately high values. In contrast, metagabbro-diorite (MGD) and metavolcanics (MVs) showed consistently lower reflectance, with a gradual decreasing trend across the spectral range. Despite these distinctions, spectral profile analysis revealed significant similarity in spectral behavior among most of the classified lithological units—most notably between metagabbro-diorite and metavolcanics—which displayed the highest degree of spectral similarity (Figure 4B). This pronounced spectral resemblance emphasizes the need for careful evaluation when interpreting the classification results for these units.
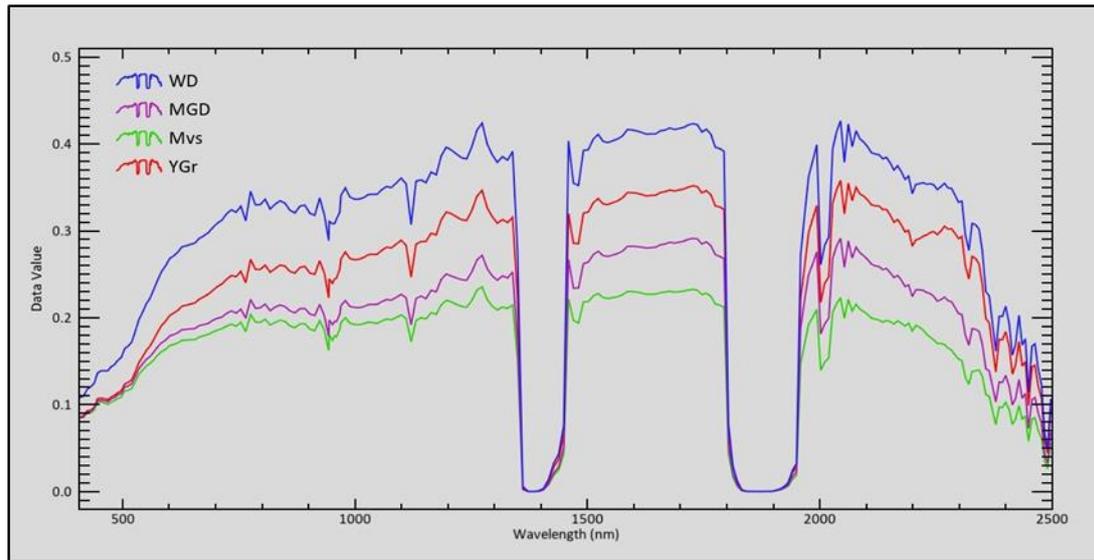
(a) The spectral profiles of the 4 rock unit classes
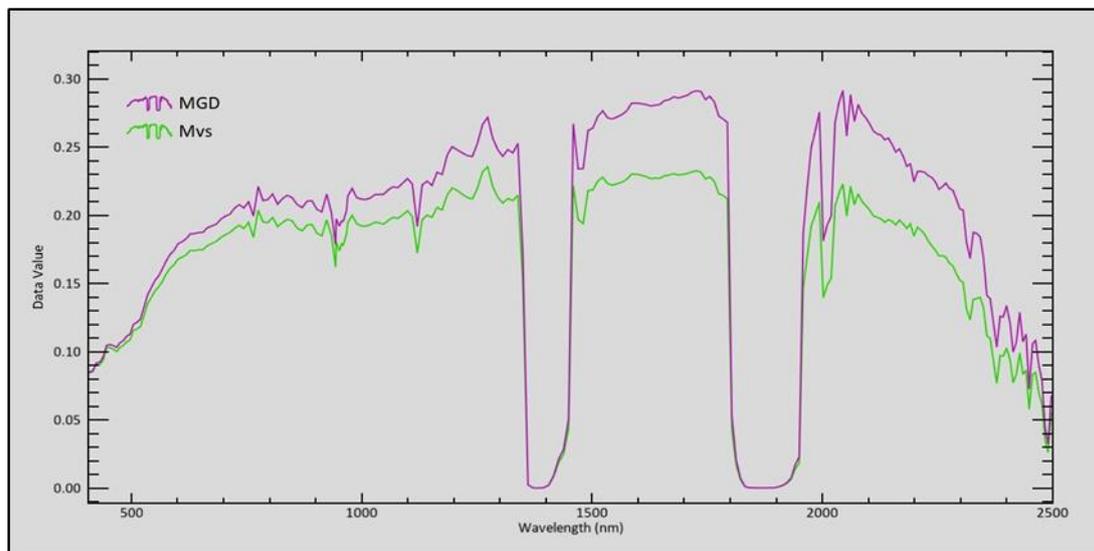
(b) High similarity in the spectral attitude of the MGD and Mvs rock units

Figure 4. The spectral profiles.

3.4. Principal Component Analysis (PCA):

Principal Component Analysis (PCA) is a technique used to reduce redundancy in correlated data through mathematical transformation [47]. In N-dimensional datasets, PCA typically encompasses around 90% of the information in the first two or three components [48]. The first component captures the largest variance, the second the next highest, and so on, producing uncorrelated outputs. PCA serves as a dimensionality reduction technique, minimizes spectral noise, enhances lithological class discrimination, and helps identify the most relevant spectral information for optimized geological analysis [28]. Principal Component

(PC) bands accumulate most of the variance available in the original bands in the higher-order PC bands and segregate the noise in the last ones. This makes the spectral differences between objects more distinguishable in individual PC images of higher orders (e.g., the first, the second, and the third PCs) than in the corresponding original bands [49]. Consequently, in the current study, PCA was applied to the PRISMA VNIR-SWIR spectral bands, yielding 234 informative PC bands. After a thorough evaluation of the resulting PCs, the first four components (PC1-PC4; Figure 5) were found to provide a rich information representation of the PRISMA hyperspectral dataset, facilitating the delineation of lithological boundaries and identification of

key spectral features for further classification and mapping efforts. PC1 captured the highest proportion of the total spectral variance in the dataset, primarily representing overall scene brightness or albedo variations. PC2 accounted for a lower, yet still meaningful, portion of the total variance. This component highlights subtle spectral variations not captured by PC1. PC3 contributed significantly less variance and emphasized diagnostic SWIR absorption features. PC4, despite accounting for only a minimal share of the total variance, highlights highly specific spectral variations or residual noise. These PCs were selected as the data input for classification using machine learning (ML) algorithms. These four PCs collectively explain approximately 99.8% of the total data variance, ensuring optimal input for the subsequent classification process. This approach aligns with Shebl et al. [13] and Shebl and Csámer [50], who provided intense testing for the performance of several machine learning algorithms in lithological discrimination. They tested these algorithms on multisource remote sensing datasets, including the first four PCs of PRISMA hyperspectral data. Their findings demonstrated the superiority of PRISMA's first four PCs compared to other PC combinations when integrated with SVM.

3.5. Lithological Classification Techniques:
3.5.1. Support Vector Machine:

Support Vector Machine (SVM) algorithm is a widely recognized as one of the most robust supervised machine learning classifiers for multiclass generalization in complex remote sensing applications [51,52]. Originally introduced by Boser et al. [53] and Cortes and Vapnik [54] within the framework of statistical learning theory, SVM constructs an optimal hyperplane that maximizes the margin between classes, thereby enhancing the separation of lithological units and providing clear class segregation.

In this study, the SVM classifier was implemented on PCA-processed PRISMA hyperspectral data. Parameter optimization for the SVM classifier was conducted in accordance with established approaches [27, 52, 55-57], with particular emphasis on the careful selection of training samples, which is critical for achieving accurate classification results [58]. Training and testing samples were selected based on PCA-transformed data supplemented by field ground control points and existing geological maps.

Moreover, the ratio of training data to testing data was maintained at 75-80% for training and 20-25% for testing (Table 1). This ratio was validated by several lithological mapping studies using SVM and similar classifiers [26, 27, 50].

To address the nonlinear spectral relationships among lithological classes, a Radial Basis Function (RBF) kernel was employed [59], enhancing class discrimination and reducing classification error [60]. Critical model parameters were optimized, with the penalty parameter set to 100 and the gamma parameter set to 0.323. These values, along with the training dataset, were used to execute the final SVM classification for the four mapped lithological classes.

3.5.2. Artificial Neural Networks:

An artificial neural network is a "computational mechanism able to acquire, represent, and compute a mapping from one multivariate space of information to another, given a set of data representing that mapping" [61]. Artificial Neural Networks (ANNs) are particularly well-suited for simulating biological neural systems and modeling complex pattern recognition tasks through networks of interconnected neurons that process weighted inputs to achieve accurate classification [62]. Their application in remote sensing is widespread, particularly for discriminating spectrally similar lithological units [63], as their multilayer architecture facilitates the extraction of hierarchical data representations, thereby improving lithological interpretation and classification.

There are two stages involved in using a neural network for accurate data classification: the training stage, in which internal connection weights are adjusted. In the current study, the widely used back-propagation algorithm was employed for training the network. This algorithm operates by performing forward and backward computations and is trained using a set of input-output training examples, adjusting weights iteratively until some targeted minimal error is achieved between the actual output and the target output values of the network. This learning algorithm consists of three layers: input, hidden, and output. Once the training is complete, the network functions as a feed-forward model to classify the entire dataset [64]. A feed-forward Multi-Layer Perceptron (MLP) with a single hidden layer was implemented, following the structure described by Venables and Ripley [65].
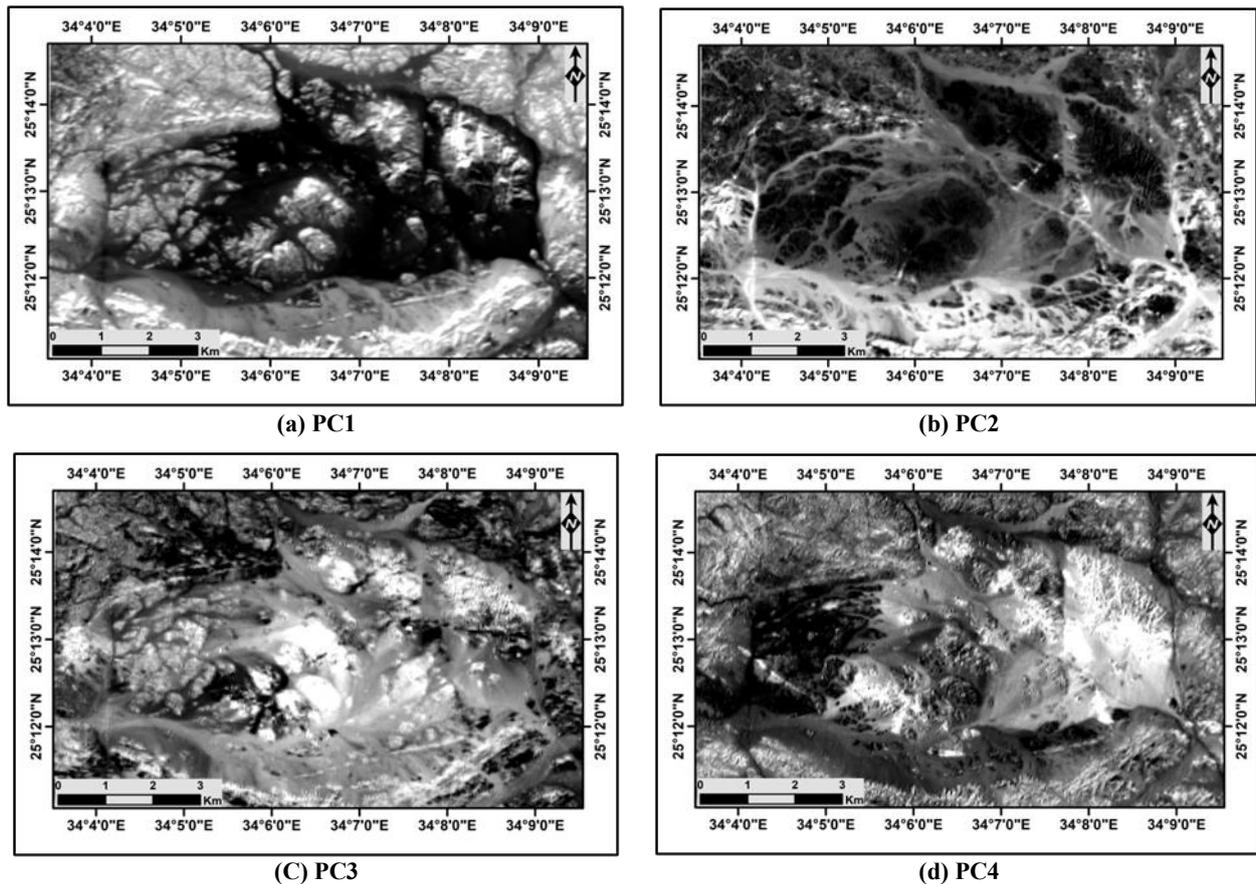
(a) PC1	(b) PC2
(C) PC3	(d) PC4

Figure 5. The First four Principal Component bands (PC1, PC2, PC3 and PC4)

3.6. Accuracy assessment:

The accuracy of lithological classification results obtained from both the Support Vector Machine (SVM) and Artificial Neural Network (ANN) algorithms was assessed using several standard evaluation metrics: the Kappa Coefficient (KC), Overall Accuracy (OA), and the precision, recall, and F1-score, all derived from the confusion matrix applied to the test dataset. The Kappa Coefficient is a powerful statistic used to compare the differences between diverse error matrices [66], particularly when dealing with categorical or qualitative data. It assesses the similarity between the classification map and reference data by considering the entire contingency matrix [17], providing a more robust measure of classification consistency than OA alone. A Kappa coefficient value closer to 1 indicates strong agreement between the classification map and reference data, while a value close to 0 suggests that agreement is no better than random chance. In parallel, OA was determined as the proportion of correctly classified pixels (represented by the diagonal elements of the confusion matrix) relative to the total number of test pixels. Additionally, precision, recall, and F1-score were employed to further evaluate classifier performance. Precision reflects the proportion of true positive predictions, whereas recall measures the model's ability to capture all actual positives. The F1-score, as the harmonic mean of precision and recall, balances both aspects of accuracy. These performance metrics are concisely presented in Table 2 and were used together to assess how well the classification methods worked for lithological mapping in the study area.

Table 1. Total number of training and testing pixels generated for different rock units

Class	Total training and testing pixels	Training pixels	Testing pixels
MGD	22815	17340 (76.00%)	5475 (24.00%)
Mvs	7766	6212 (79.99%)	1554 (20.01%)
YGr	10352	8072 (77.99%)	2278 (22.01%)

3.7. Validation:

Fieldwork and petrographic analysis formed the main components of this study's verification process. Comprehensive field validations, along with petrographic analysis, were systematically conducted to verify the classification results through ground-truth data collection and thin-section examination. The validation process involved rigorous comparison between model outputs and actual geological observations, with particular attention given to analyzing classification errors and refining the model to improve accuracy for challenging lithological units. Through iterative adjustments based on field evidence and microscopic analysis, the classification approach was progressively optimized. The final lithological map, validated against field data, petrographical analysis, and established regional geological knowledge, offers a robust and reliable representation of the geology of the study area that integrates remote sensing analysis with traditional geological verification methods.

Table 2. Performance metrics and their formula

| Performance metrics	Formula
Kappa Coefficient (KC)	$KC = (Po – Pe) / (1 – Pe)$
Overall Accuracy (OA)	$OA = (TP + TN) / (TP + TN + FP + FN) \times 100\%$
Precision	$Precision = TP / (TP + FP)$
Recall	$Recall = TP / (TP + FN)$
F1-score	$F1\text{-}score = 2 \times (Precision \times Recall) / (Precision + Recall)$
Where: $Po = (TP + TN) / (TP + TN + FP + FN)$ $Pe = [(TP + FP)(TP + FN) + (FN + TN)(FP + TN)] / (TP + TN + FP + FN)^2$	

4. Results and discussion:
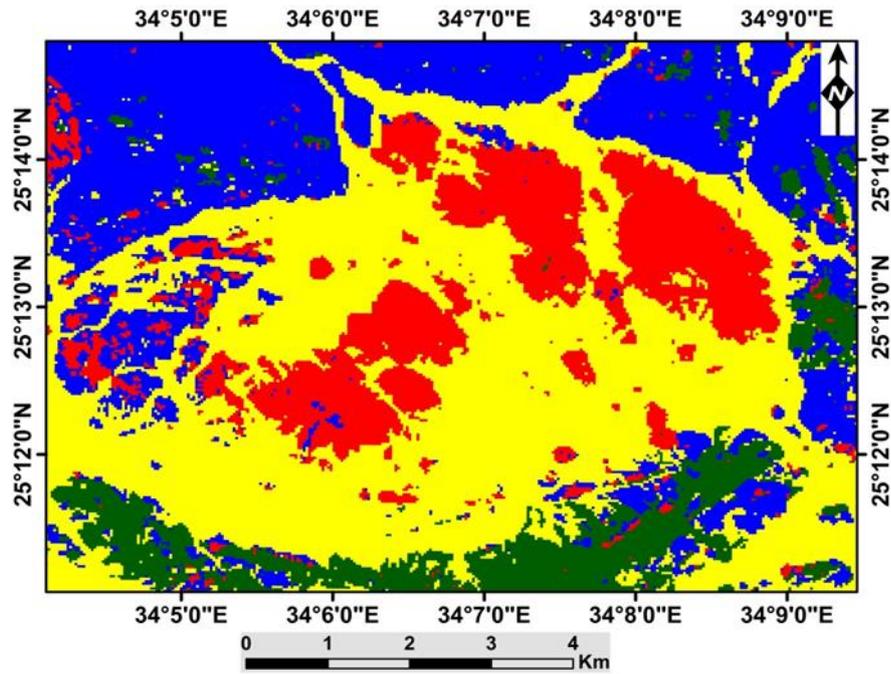### 4.1. Classification Maps:

The classification results produced by the SVM (Figure 6A) and the ANNs (Figure 6B) successfully illustrate the spatial distribution of lithological units within the study area. Both methods exhibit strong discriminative performance across nearly all mapped classes, thereby confirming the effectiveness of the adopted algorithms in differentiating various rock types. This is further supported by the high overall accuracy (OA) values and substantial Kappa coefficient (KC) scores achieved. Furthermore, the classification accuracy was quantitatively assessed using confusion matrices for both SVM and ANN results (Table 3 and Table 4, respectively). From these, key performance metrics, including OA, KC, precision, recall, and F1-score, were derived and are collectively summarized in Table 5, offering a comprehensive evaluation of each model's performance.

The SVM classification achieved a high overall accuracy (OA) of 93.88%, with a corresponding Kappa Coefficient (KC) of 0.9102. Similarly, the ANN classification produced an OA of 92.01% and a KC of 0.8828. Although visual inspection of the classified lithological maps (Figure 6A and 6B) confirms excellent discrimination of wadi deposits and younger granite units, the metavolcanics and metagabbro-diorite complex exhibited notable intercalation, resulting in comparatively lower classification accuracy for these classes, aligning with earlier concerns raised by their spectral signature profiles. This notable intercalation between the metagabbro-diorite complex and metavolcanics can be attributed to their close spatial association and shared high-grade metamorphic history, which has locally altered their mineralogical compositions, producing similar metamorphic products in both units. These observations are quantitatively confirmed by the performance matrices presented in Table 5, where the metavolcanics class showed an F1-score of 0.8049 and 0.7814 in both SVM and ANN classifiers, respectively, while the metagabbro-diorite complex class achieved a higher F1-score of 0.9382 and 0.9156 for SVM and ANNs, respectively. In contrast, the wadi deposits class demonstrated exceptional classification performance, with F1-score values of 0.9722 and 0.9620% for SVM and ANNs, respectively. Similarly, the younger granite class showed relatively high F1-score values of 0.9391% and 0.9061% for SVM and ANNs, respectively, indicating strong model performance for these units.
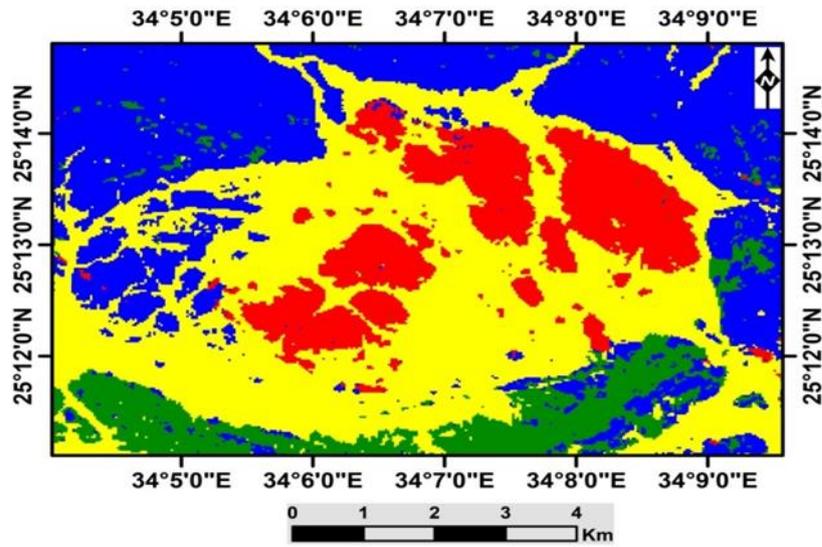
(a) Lithological classification result using SVM

(b) Lithological classification result using ANN

Figure 6. Lithological classification results

Table 3. Confusion matrix of the SVM classification algorithm results based on testing data.

Class	MGD	Mvs	YGr	WD	Total
MGD	5063	155	53	47	5318
Mvs	376	1310	4	11	1701
YGr	15	4	2152	134	2305
WD	21	85	69	6413	6588
Total	5475	1554	2278	6605	15912

Table 4. Confusion matrix of the ANN classification algorithm results based on testing data.

Class	MGD	Mvs	YGr	WD	Total
MGD	4874	202	32	63	5171
Mvs	385	1253	0	15	1653
YGr	105	43	2122	136	2406
WD	111	56	124	6391	6682
Total	5475	1554	2278	6605	15912

Table 5. Accuracy assessment metrics for lithological classification produced using SVM and ANNs algorithms applied to PRISMA hyperspectral data.

ML	SVM			ANN		
class	Precision	Recall	F1-score	Precision	Recall	F1-score
MGD	0.9520	0.9247	0.9382	0.9426	0.8902	0.9156
Mvs	0.7701	0.8430	0.8049	0.7580	0.8063	0.7814
YGr	0.9336	0.9447	0.9391	0.8820	0.9315	0.9061
WD	0.9734	0.9709	0.9722	0.9565	0.9676	0.9620
OA	93.88%			92.01%		
KC	0.9102			0.8828		

4.2. The final lithological map:

The final lithological map (Figure 7) was developed using ArcGIS software by integrating multiple data sources, including PRISMA-based SVM and ANN classification outputs, previous geological maps, field control points, and petrographic analyses. Initially, previous maps were digitized and georeferenced to establish a preliminary framework. Machine learning-based lithological classifications were overlaid and compared with ground truth data collected during field surveys. Petrographic analysis of representative samples further validated rock unit identification, particularly in zones of spectral ambiguity. Lithological boundaries were manually refined using ArcMap's editing tools, with careful adjustments informed by expert interpretation and spectral characteristics. Each mapped unit was assigned appropriate attributes and standardized symbology. The final map was validated through cross-referencing with field observations and prior geological knowledge to ensure geological consistency and spatial accuracy.

The resulting lithological map reveals that the study area encompasses key lithological components and rock assemblages characteristic of the Egyptian-Nubian Shield (ENS) and likely across the broader Arabian-Nubian Shield (ANS). The successfully identified and mapped lithological units comprise four dominant lithological groups: (1) island arc metavolcanics, (2) metagabbro-diorite complex, (3) younger granites, and (4) wadi deposits. This detailed mapping of Precambrian rocks effectively resolves the inconsistencies in earlier geological map of the area (Figure 1C), which were limited by subjective interpretation and the inherent constraints of traditional field-based mapping methods.

The lithological map produced in this study generally aligns with the previous geological map (Figure 1C) in identifying four principal lithological units within the study area, including metavolcanics, metagabbro-diorite complex, younger granites, and wadi deposits. However, notable discrepancies exist in the lithological interpretation of specific regions.

In the earlier map, two additional rock types, serpentinites and older granites, were mapped in several locations. However, these units were re-evaluated in the current study and found to be misclassified. Field verification and petrographic analysis, along with remote sensing analysis, revealed that the areas previously labeled as serpentinites in Figure 1C are actually sheared metavolcanics exposed in the southern part of the mapped area. Similarly, areas previously mapped as older granites in the earlier map (Figure 1C) were confirmed to be dioritic phases belonging to the metagabbro-diorite suite. These findings highlight the improved lithological resolution and classification accuracy achieved in the present study through the integration of hyperspectral datasets and advanced MLAs. Consequently, the revised map corrects key inaccuracies present in earlier works, offering improved spatial accuracy. It also emphasizes the importance of integrating high-resolution spectral data, robust machine learning techniques, and expert geological knowledge for refining lithological mapping in complex Precambrian terranes.
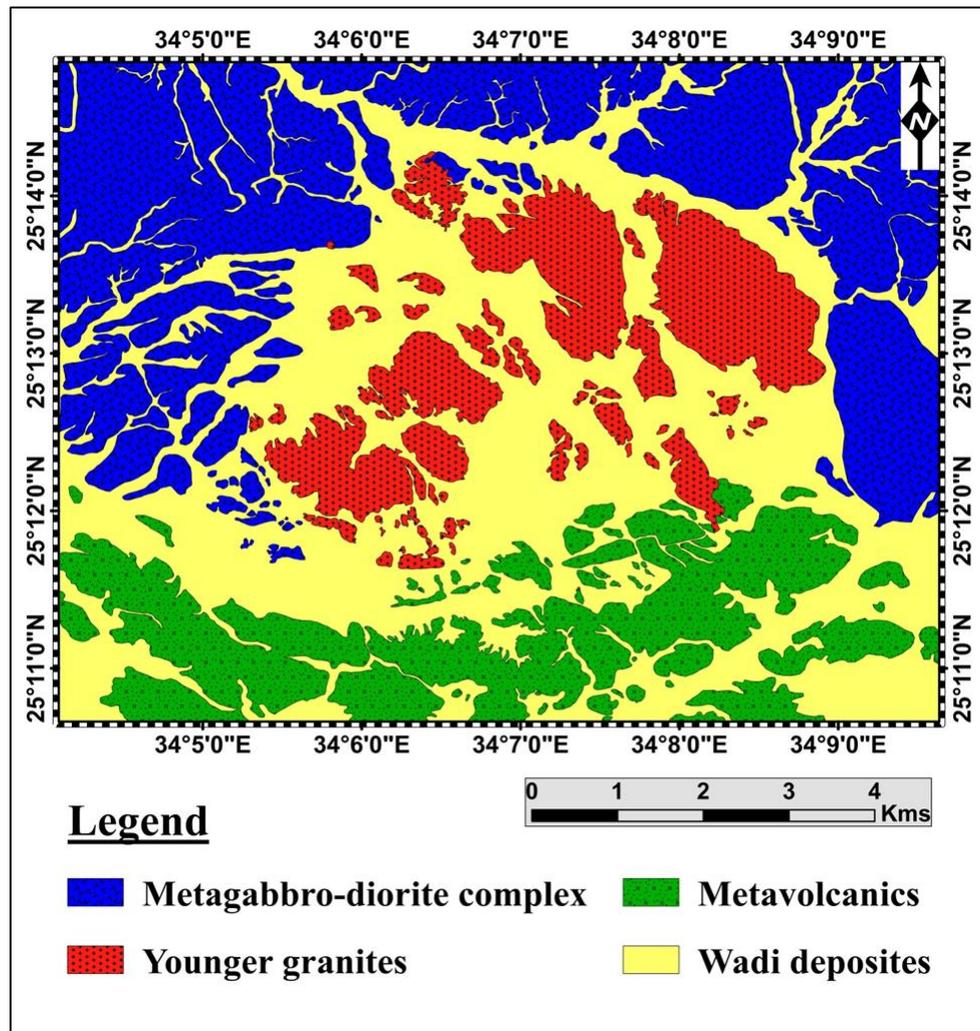
Figure 7. Detailed lithological map of the El Ineigi area obtained from the present work.

5. Verification

In addition to the statistical accuracy assessment, visual interpretation, and comparison with previous geological maps, the produced lithological map was further verified, validated, and cross-referenced with our field investigations and petrographic analysis. This multi-method validation approach served to confirm the spatial accuracy of classified lithological units through direct field observation, verify mineralogical composition via microscopic analysis of representative samples, and identify potential misclassification patterns through detailed error analysis.

During fieldwork, a substantial number of GPS-referenced observation stations were examined, with:

particular emphasis on the verification of lithological contacts, detailed description of rock units, and analysis of structural features. As illustrated in Figure 8, representative field observation points demonstrated strong agreement between the mapped lithological units and the actual rock exposures, confirming that the rock units observed in the field locations closely matched the predictions of the final lithological map. For further validation, field photographs of key lithological units from the study area are presented in Section 2 with their locations indicated in Figure 8 to facilitate precise identification and confirmation.

Furthermore, representative photomicrographs of the main lithological units identified within the study area are introduced in Figure 9 to facilitate better identification and validation. This agreement enhances our results and recommends the adopted approach for further lithological mapping in similar terrains.
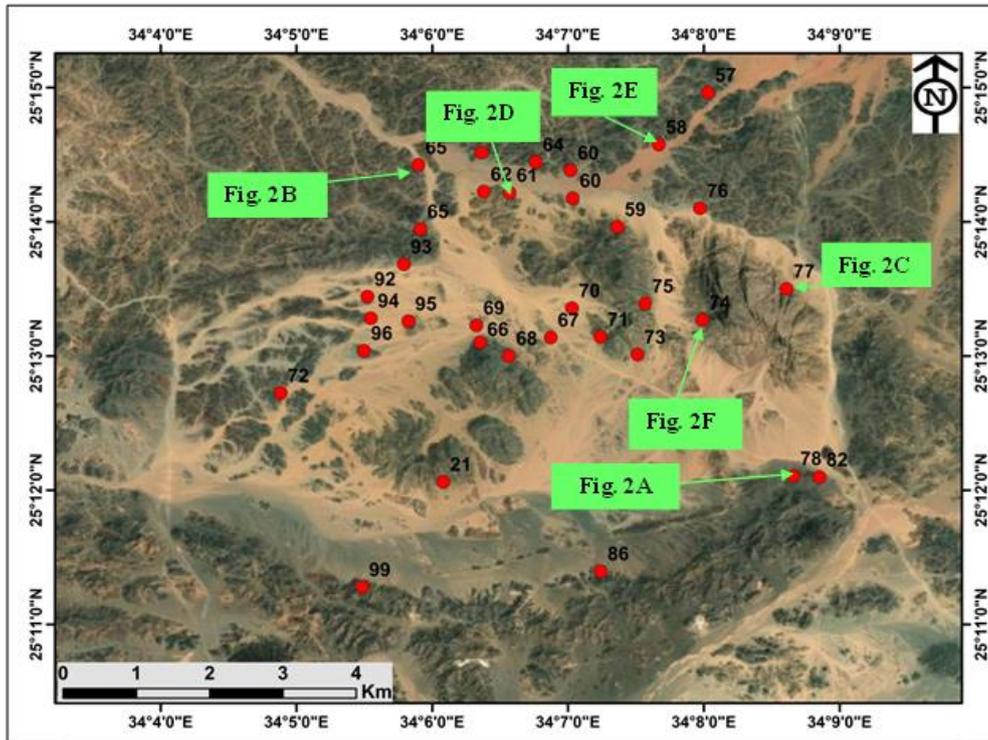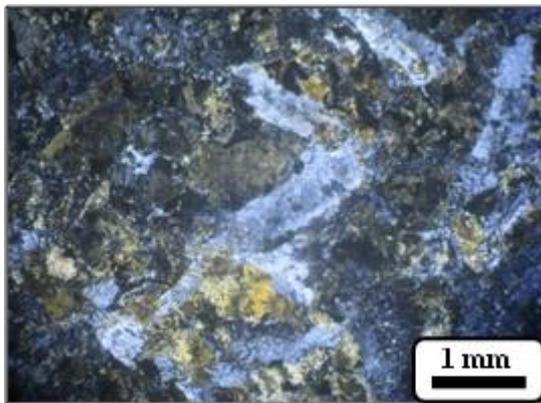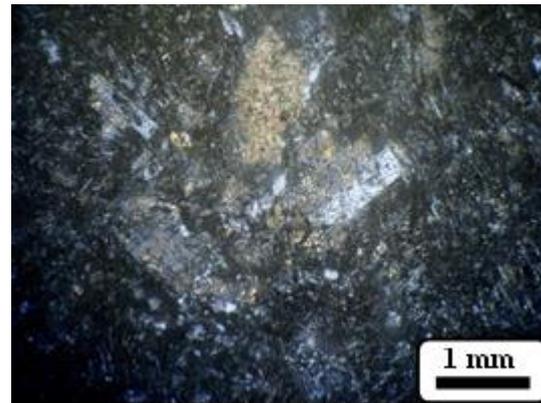
13

Figure 8. Satellite image of the study area showing the spatial distribution of field observation points and the locations of field photographs. Map created by ArcGIS Desktop v 10.8.
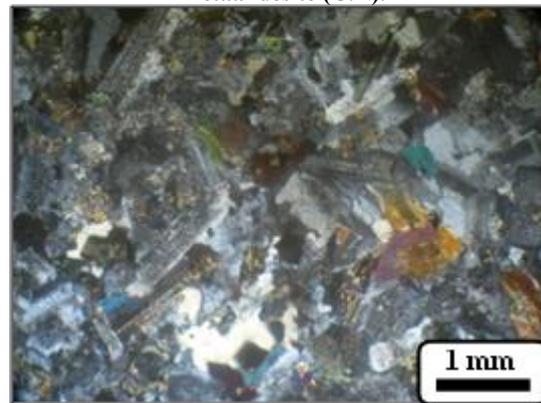

(a) General view in intergranular metabasalt showing partially altered augite and plagioclase crystals (C.N)

(b) Porphyritic texture with phenocrysts of completely and partially altered plagioclase to calcite in porphyritic metaandesite (C.N).
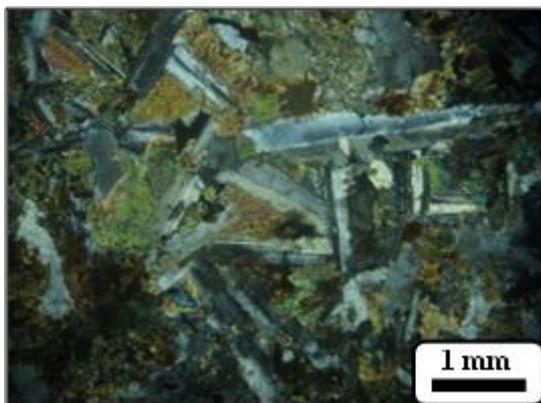
(c) General view in metagabbro consists of plagioclase, altered augite, hornblende and biotite with minor quartz (C.N).

(d) General view of diorite showing partially altered plagioclase, hornblende and biotite with minor quartz (C.N).

(e) General view showing perthitic texture in alkali feldspar granite (C.N.).

(f) Graphic and granophyric textures in alkali feldspar granite (C.N.).

Figure 9. microphotographs

6. Conclusions

This contribution proposes an innovative integrated approach for effective lithological mapping of the El Ineigi area in the CED of Egypt. Our approach combines PRISMA hyperspectral satellite imagery classification using SVM and ANN classification algorithms guided by training data derived from Principal Component Analysis (PCA), enabling accurate definition of the spatial distribution of various rock units within the study area. The study concludes the following points:

1. This research represents the first successful application of PRISMA hyperspectral data coupled with SVM and ANN machine learning algorithms to generate a new lithological map of the study area with an overall accuracy up to 93.88% for SVM and 92.01% for ANN classifiers. The results address inconsistencies resulting from subjective interpretations in conventional mapping approaches and fill the gap in detailed geological mapping of the El Ineigi area.

2. The results demonstrate the exceptional capability of this approach in discriminating between different rock units exposed in the mapped area, including island arc metavolcanics, syntectonic metagabbro-diorite complex, younger granites, and wadi deposits. Fieldwork and petrographic investigations validate the findings to ensure accuracy and reliability.

3. PCAs transformations (especially the first four PCAs) contributed significantly by reducing noise and enhancing spectral information, which proved essential for accurately distinguishing between lithologies and efficiency in detailed lithological mapping.

4. After comparative visual interpretation with existing geological maps, extensive field investigations, and comprehensive statistical analysis, the proposed methodological framework in the current research proves highly effective. As a result, we strongly recommend being followed for further lithological discrimination in similar geological terrains across the Arabian-Nubian Shield (ANS), particularly due to the ability of the current approach to resolve subtle relationships between closely associated rock types within the same exposures, as confirmed by our field observations.

Declarations

Conflicts of interest/Competing interests: the authors declare that they have no known competing financial interests or personal relationships that could have appeared to influence.

References

[1]. Chattoraj, S. L., Prasad, G., Sharma, R. U., van der Meer, F. D., Guha, A., & Pour, A. B. (2020). Integration of remote sensing, gravity and geochemical data for exploration of Cu-mineralization in Alwar basin, Rajasthan, India. *International Journal of Applied Earth Observation and Geoinformation*, *91*, 102162.

[2]. Marquina Araujo, J. J., Cotrina Teatino, M. A., Mamani Quispe, J. N., Noriega Vidal, E. M., Vega Gonzalez, J. A., Vega-Gonzalez, J., & Cruz-Galvez, J. (2024). Copper ore grade prediction using machine learning techniques in a copper deposit. *Journal of Mining and Environment*, *15*(3), 1011-1027.

[3]. Pei, T., Xu, J., Liu, Y., Huang, X., Zhang, L., Dong, W., ... & Zhou, C. (2021). GIScience and remote sensing in natural resource and environmental research: Status quo and future perspectives. *Geography and Sustainability*, *2*(3), 207-215.

[4]. Cotrina Teatino, M. A., Marquina Araujo, J. J., & Mamani-Quispe, J. N. (2025). Application of artificial neural networks for the categorization of mineral resources in a copper deposit in Peru. *World Journal of Engineering*.

[5]. Cotrina Teatino, M. A., Marquina Araujo, J. J., Noriega Vidal, E. M., Mamani Quispe, J. N., Ccatamayo Barrios, J. H., Gonzalez Vasquez, J. A., & Arango Retamozo, S. M. (2024). Predicting open pit mine production using machine learning techniques: A case study in Peru. *Journal of Mining and Environment*, *15*(4), 1345-1355.

[6]. Ambrosino, A., Di Benedetto, A., & Fiani, M. (2023). LiDAR Data and HRSI to Evaluate the Mitigating Effect of Forests into Rockfall Risk Analysis Using SOM: Mt San Liberatore Case Study. *Remote Sensing*, *15*(18), 4523.

[7]. Zhong, A., Wang, Z., Zhang, Z., & Hu, C. (2024). Remote sensing monitoring of ecological environment quality in mining areas under the perspective of ecological engineering. *Environmental Earth Sciences*, *83*(20), 587.

[8]. Houshmand, N., GoodFellow, S., Esmaeili, K., & Calderón, J. C. O. (2022). Rock type classification based on petrophysical, geochemical, and core imaging data using machine and deep learning techniques. *Applied Computing and Geosciences*, *16*, 100104.

[9]. Madsen, R. B., Høyer, A. S., Sandersen, P. B., Møller, I., & Hansen, T. M. (2023). A method to construct statistical prior models of geology for probabilistic inversion of geophysical data. *Engineering Geology*, *324*, 107252.

[10]. El-Omairi, M. A., & El Garouani, A. (2023). A review on advancements in lithological mapping utilizing machine learning algorithms and remote sensing data. *Heliyon*, *9*(9).

[11]. Rezaei, A., Hassani, H., Moarefvand, P., & Golmohammadi, A. (2020). Lithological mapping in Sangan region in Northeast Iran using ASTER satellite data and image processing methods. *Geology, Ecology, and Landscapes*, *4*(1), 59-70.

[12]. Asadzadeh, S., Koellner, N., & Chabrillat, S. (2024). Detecting rare earth elements using EnMAP hyperspectral satellite data: a case study from Mountain Pass, California. *Scientific Reports*, *14*(1), 20766.

[13]. Shebl, A., Abriha, D., Fahil, A. S., El-Dokouny, H. A., Elrasheed, A. A., & Csámer, Á. (2023). PRISMA hyperspectral data for lithological mapping in the Egyptian Eastern Desert: Evaluating the support vector machine, random forest, and XG boost machine learning algorithms. *Ore Geology Reviews*, *161*, 105652.

[14]. Matsunaga, T., Tachikawa, T., & Kashimura, O. (2023, July). An Overview of Geologic and Environmental Applications of HISUI. In *IGARSS 2023-2023 IEEE International Geoscience and Remote Sensing Symposium* (pp. 4674-4675). IEEE.

[15]. Mishra, G., Govil, H., Guha, A., Kumar, H., Kumar, S., & Mukherjee, S. (2024). Comparative evaluation of airborne AVIRIS-NG and spaceborne PRISMA hyperspectral data in identification and mapping of altered/weathered minerals in Jahazpur, Rajasthan. *Advances in Space Research*, *73*(2), 1459-1474.

[16]. Tripathi, P., & Garg, R. D. (2023). Potential of DESIS and PRISMA hyperspectral remote sensing data in rock classification and mineral identification: a case study for Banswara in Rajasthan, India. *Environmental Monitoring and Assessment*, *195*(5), 575.

[17]. Cracknell, M. J., & Reading, A. M. (2014). Geological mapping using remote sensing data: A comparison of five machine learning algorithms, their response to variations in the spatial distribution of training data and the use of explicit spatial information. *Computers & Geosciences*, *63*, 22-33.

[18]. Shebl, A., Kusky, T., & Csámer, Á. (2022). Advanced land imager superiority in lithological classification utilizing machine learning algorithms. *Arabian Journal of Geosciences*, *15*(9), 923.

[19]. Suthaharan, S. (2016). Support vector machine. In *Machine learning models and algorithms for big data classification: thinking with examples for effective learning*. Boston, MA: Springer US, 207-235.

[20]. Liu, H., Zhang, H., & Yang, R. (2024). Lithological Classification by Hyperspectral Remote Sensing Images Based on Double-Branch Multi-Scale Dual-Attention Network. *IEEE Journal of Selected Topics in Applied Earth Observations and Remote Sensing*.

[21]. Manap, H. S., & San, B. T. (2022). Data integration for lithological mapping using machine learning algorithms. *Earth Science Informatics*, *15*(3), 1841-1859.

[22]. Kumar, C., Chatterjee, S., Oommen, T., & Guha, A. (2020). Automated lithological mapping by integrating spectral enhancement techniques and machine learning algorithms using AVIRIS-NG hyperspectral data in Gold-bearing granite-greenstone rocks in Hutti,

India. *International Journal of Applied Earth Observation and Geoinformation*, *86*, 102006.

[23]. El-Omairi, M. A., & El Garouani, A. (2024). Lithological Mapping using Artificial Intelligence and Remote Sensing data: A Case Study of Bab Boudir region, Morocco. In *BIO Web of Conferences* (Vol. 115, p. 01005). EDP Sciences.

[24]. Ghoneim, S. M., Hamimi, Z., Abdelrahman, K., Khalifa, M. A., Shabban, M., & Abdelmaksoud, A. S. (2024). Machine learning and remote sensing-based lithological mapping of the Duwi Shear-Belt area, Central Eastern Desert, Egypt. *Scientific Reports*, *14*(1), 17010.

[25]. Lauzon, D., & Gloaguen, E. (2024). Quantifying uncertainty and improving prospectivity mapping in mineral belts using transfer learning and Random Forest: a case study of copper mineralization in the Superior Craton Province, Quebec, Canada. *Ore Geol. Rev. 166*, 105918.

[26]. Shebl, A., & Hamdy, M. (2023). Multiscale (microscopic to remote sensing) preliminary exploration of auriferous-uraniferous marbles: A case study from the Egyptian Nubian Shield. *Scientific Reports*, *13*(1), 9173.

[27]. Abdelkader, M. A., Watanabe, Y., Shebl, A., El-Dokouny, H. A., Dawoud, M., & Csámer, Á. (2022). Effective delineation of rare metal-bearing granites from remote sensing data using machine learning methods: A case study from the Umm Naggat Area, Central Eastern Desert, Egypt. *Ore Geology Reviews*, *150*, 105184.

[28]. El-Omairi, M. A., El Garouani, M., & El Garouani, A. (2025). Enhanced lithological mapping via remote sensing: Employing SVM, random trees, ANN, with MNF and PCA transformations. *The Egyptian Journal of Remote Sensing and Space Sciences*, *28*(1), 34-52.

[29]. Agrawal, N., Govil, H., Chatterjee, S., Mishra, G., & Mukherjee, S. (2024). Evaluation of machine learning techniques with AVIRIS-NG dataset in the identification and mapping of minerals. *Advances in Space Research*, *73*(2), 1517-1534.

[30]. Cardoso-Fernandes, J., Teodoro, A. C., Lima, A., & Roda-Robles, E. (2020). Semi-automatization of support vector machines to map lithium (Li) bearing pegmatites. *Remote Sensing*, *12*(14), 2319.

[31]. Shereif, A. S., Shebl, A., Mahmoud, A. S., & Csámer, Á. (2024). Enhanced Lithological Mapping in El-Missikat and El-Erediya Areas, Central Eastern Desert, Egypt, Leveraging Remote Sensing Techniques and Machine Learning Algorithms. *IEEE Transactions on Geoscience and Remote Sensing*.

[32]. Ali-Bik, M. W., Zafar, T., Hassan, S. M., Sadek, M. F., & Abo Khashaba, S. M. (2025). Applications of machine learning algorithms in lithological mapping of Saint Katherine Neoproterozoic rocks in the South Sinai of Egypt using hyperspectral PRISMA data. *Scientific Reports*, *15*(1), 10192.

[33]. Wang, W., Xue, C., Zhao, J., Yuan, C., & Tang, J. (2024). Machine learning-based field geological mapping: A new exploration of geological survey data acquisition strategy. *Ore Geology Reviews*, *166*, 105959.

[34]. Gillfeather-Clark, T., Horrocks, T., Holden, E. J., & Wedge, D. (2021). A comparative study of neural network methods for first break detection using seismic refraction data over a detrital iron ore deposit. *Ore Geology Reviews*, *137*, 104201.

[35]. Zhang, C., Zuo, R., & Xiong, Y. (2021). Detection of the multivariate geochemical anomalies associated with mineralization using a deep convolutional neural network and a pixel-pair feature method. *Applied Geochemistry*, *130*, 104994.

[36]. Hammond, Z., & Allen, D. M. (2024). Evaluating the feasibility of using artificial neural networks to predict lithofacies in complex glacial deposits. *Hydrogeology Journal*, *32*(2), 509-526.

[37]. Soulaimani, S., Soulaimani, A., Abdelrahman, K., Miftah, A., Fnais, M. S., & Mondal, B. K. (2024). Advanced machine learning artificial neural network classifier for lithology identification using Bayesian optimization. *Frontiers in Earth Science*, *12*, 1473325.

[38]. Shirmard, H., Farahbakhsh, E., Heidari, E., Beiranvand Pour, A., Pradhan, B., Müller, D., & Chandra, R. (2022). A comparative study of convolutional neural networks and conventional machine learning models for lithological mapping using remote sensing data. *Remote Sensing*, *14*(4), 819.

[39]. Li, T., Zuo, R., Zhao, X., & Zhao, K. (2022). Mapping prospectivity for regolith-hosted REE deposits via convolutional neural network with generative adversarial network augmented data. *Ore Geology Reviews*, *142*, 104693.

[40]. Latifovic, R., Pouliot, D., & Campbell, J. (2018). Assessment of convolution neural networks for surficial geology mapping in the South Rae geological region, Northwest Territories, Canada. *Remote sensing*, *10*(2), 307.

[41]. Priyadarshini, K.N., Sivashankari, V., Shekhar, S., & Balasubramani, K. (2019). Comparison and Evaluation of Dimensionality Reduction Techniques for Hyperspectral Data Analysis, in: *The 2nd International Electronic Conference on Geosciences*, *MDPI*, p. 6.

[42]. Stern, R.J., & Ali, K. (2020). Crustal evolution of the Egyptian Precambrian rocks. In: *The geology of Egypt* (pp 131–151). Cham: Springer International Publishing.

[43]. Mohamed, F.H., & El-Sayed, M.M. (2008). Post-orogenic and anorogenic A-type fluorite-bearing granitoids, Eastern Desert, Egypt: petrogenetic and geotectonic implications. *Geochemistry*, *68*(4), 431-450.

[44]. Bedini, E., & Chen, J. (2020). Application of PRISMA satellite hyperspectral imagery to mineral alteration mapping at Cuprite, Nevada, USA. *Journal of hyperspectral remote sensing*, *10*(2), 87-94.

[45]. Loizzo, R., Daraio, M., Guarini, R., Longo, F., Lorusso, R., Dini, L., & Lopinto, E. (2019) PRISMA mission status and perspective. In *IGARSS 2019-2019 IEEE International Geoscience and Remote Sensing Symposium*, Yokohama, Japan (4503-4506).

[46]. Loizzo, R., Guarini, R., Longo, F., Scopa, T., Formaro, R., Facchinetti, C., & Varacalli, G. (2018). PRISMA: The Italian hyperspectral mission. In *IGARSS 2018-2018 IEEE international geoscience and remote sensing symposium* (pp. 175-178). IEEE.

[47]. Caloz, R., & Collet, C. (2001). Digital remote sensing image processing. Remote Sensing Pulled Silkscreen-Presses de l'Université du Québec, 3, 381.

[48]. Jia, X., & Richards, J. A. (1999). Segmented principal components transformation for efficient hyperspectral remote-sensing image display and classification. *IEEE transactions on Geoscience and Remote Sensing*, *37*(1), 538-542.

[49]. Sabins, F. F. (1999). Remote sensing for mineral exploration. *Ore Geol. Rev. 14*, 157–183.

[50]. Shebl, A., & Csámer, Á. (2021). Stacked vector multi-source lithologic classification utilizing Machine Learning Algorithms: Data potentiality and dimensionality monitoring. *Remote Sensing Applications: Society and Environment*, 24, 100643.

[51]. Shebl, A., Abdellatif, M., Hissen, M., Abdelaziz, M. I., & Csámer, Á. (2021). Lithological mapping enhancement by integrating Sentinel 2 and gamma-ray data utilizing support vector machine: A case study from Egypt. *International Journal of Applied Earth Observation and Geoinformation*, *105*, 102619.

[52]. Ougiaroglou, S., Diamantaras, K. I. & Evangelidis, G. (2018). Exploring the effect of data reduction on Neural Network and Support Vector Machine classification. *Neurocomputing*, *280*, 101-110.

[53]. Boser, B. E., Guyon, I. M. & Vapnik, V. N. (1992). A training algorithm for optimal margin classifiers. In *Proceedings of the fifth annual workshop on Computational learning theory*, 144-152. 1

[54]. Cortes, C., & Vapnik, V. (1995). Support-vector networks. *Machine learning*, *20*, 273-297.

[55]. Cotrina, M., Marquina, J., Mamani, J., Arango, S., Gonzalez, J., Noriega, E., & Antonio, E. (2025). Hybrid machine learning techniques to predict fuel consumption of dump trucks in an open-pit mine in Peru. *International Journal of Mining and Mineral Engineering*, *16*(1), 1-20.

[56]. Kranjčić, N., Medak, D., Župan, R., & Rezo, M. (2019). Support vector machine accuracy assessment for extracting green urban areas in towns. *Remote sensing*, *11*(6), 655.

[57]. Othman, A. A., & Gloaguen, R. (2014). Improving lithological mapping by SVM classification of spectral and morphological features: The discovery of a new chromite body in the Mawat ophiolite complex (Kurdistan, NE Iraq). *Remote Sensing*, *6*(8), 6867-6896.

[58]. Sebtosheikh, M. A., Motafakkerfard, R., Riahi, M. A., Moradi, S., & Sabety, N. (2015). Support vector machine method, a new technique for lithology prediction in an Iranian heterogeneous carbonate reservoir using petrophysical well logs. *Carbonates and evaporites*, *30*, 59-68.

[59]. Petropoulos, G. P., Kalaitzidis, C., & Prasad Vadrevu, K. (2012). Support vector machines and object-based classification for obtaining land-use/cover cartography from Hyperion hyperspectral imagery. *Comput. Geosci. 41*, 99–107.

[60]. Vapnik, V. N. (1995). *The Nature of Statistical Learning Theory*. Springer Nature, New York, NY.

[61]. Garrett, J. H. (1994). Where and why artificial neural networks are applicable in civil engineering. *Journal of Computing in Civil Engineering*, *8*, 129-130.

[62]. Hastie, T., Tibshirani, R., Friedman, J., & Franklin, J. (2005). The elements of statistical learning: data mining, inference and prediction. *The Mathematical Intelligencer*, *27*(2), 83-85.

[63]. Haykin, S. (2009). *Neural Networks and Learning Machines*. Third Edition, Pearson Education, Inc., McMaster University, Hamilton.

[64]. Lee, S., Ryu, J. H., & Kim, I. S. (2007). Landslide susceptibility analysis and its verification using likelihood ratio, logistic regression, and artificial neural network models: case study of Youngin, Korea. *Landslides*, *4*, 327-338.

[65]. Venables, W. N., & Ripley, B. D. (2002). *Modern Applied Statistics with S*, 4th Edition, Springer Science, New York, USA.

[66]. Viera, A. J., & Garrett, J. M. (2005). Understanding interobserver agreement: the kappa statistic. *Fam med*, *37*(5), 360-36.

به سوی نقشه‌برداری پیشرفته زمین‌شناسی از سنگ‌های پرکامبرین در منطقه ال اینیجی، صحرای مرکزی شرقی، مصر: ادغام داده‌های ماهواره‌ای فراطیفی و الگوریتم یادگیری ماشین

احمد ام. عبدالحمید‎١,٢*، ماهر الاموی‎٣، ایمن محروس‎١,٤، محمد ای. الخولی‎٥ و عادل فتحی‎١۶

١. گروه محیط زیست فضایی، موسسه علوم پایه و کاربردی، دانشگاه علوم و فناوری مصر-ژاپن(E-JUST) ، شهر جدید برج العرب، اسکندریه ٢١٩٣٤، مصر

٢. گروه زمین شناسی، دانشکده علوم، دانشگاه سوهاج، سوهاج ٨٢٥٢٤، مصر

٣. گروه زمین شناسی، دانشکده علوم، دانشگاه بنها، بنها ١٣٥١٨، مصر

٤. گروه فیزیک، دانشکده علوم، دانشگاه حلوان، حلوان، قاهره ١١٧٩٥، مصر

٥. برنامه علوم نانو، موسسه علوم پایه و کاربردی، دانشگاه علوم و فناوری مصر-ژاپن(E-JUST) ، شهر جدید برج العرب، اسکندریه ٢١٩٣٤، مصر

۶. گروه فیزیک، دانشکده علوم، دانشگاه فیوم، فیوم ۶٣٥١٤، مصر

چکیده

استخراج مس پورفیری مقادیر قابل‌توجهی باطله تولید می‌کند که به دلیل توانایی در تولید اسید و آزادسازی عناصر بالقوه سمی، مخاطرات جدی زیست‌محیطی و بهداشتی برای انسان به همراه دارد. در این مطالعه، ارزیابی یکپارچه‌ای از ریسک‌های زیست‌محیطی و سلامت انسانی ناشی از باطله‌های معدن مس پورفیری سونگون در شمال‌غرب ایران ارائه شده است. بدین منظور، رویکردی جامع و میان‌رشته‌ای به کار گرفته شد که شامل ترکیب آنالیزهای فیزیکوشیمیایی، کانی‌شناسی و ژئوشیمیایی با روش‌های آماری بود. گونه‌بندی شیمیایی عناصر با استفاده از روش اصلاح‌شده پیشنهادی دفتر مرجع جامعه اروپا انجام شد؛ روشی که در مطالعات متعدد برای ارزیابی تفکیک ژئوشیمیایی و تحرک‌پذیری عناصر به کار رفته است. هدف اصلی این پژوهش، گذار از تحلیل صرف غلظت کل عناصر به سوی ارزیابی دقیق‌تر ریسک مبتنی بر زیست‌دسترس‌پذیری، با بهره‌گیری از چارچوب سازمان حفاظت محیط‌زیست ایالات متحده برای کودکان و بزرگسالان بود. بررسی‌های کانی‌شناسی نشان داد که باطله‌ها دارای پتانسیل خالص تولید اسید هستند، به‌گونه‌ای که مقدار پیریت (حدود ۴ درصد) معمولاً بیش از کانی خنثی‌کننده اصلی، یعنی کلسیت (حدود ٢ درصد)، است. نتایج آنالیزهای ژئوشیمیایی بیانگر غنی‌شدگی قابل‌توجه مس و مولیبدن و همچنین غنی‌شدگی متوسط آرسنیک و کبالت در باطله‌ها بود. در میان عناصر مورد بررسی، بیشترین ضرایب تحرک به ترتیب متعلق به مس (٨١,۴٩٪)، سرب (٧۶,٧١٪)، روی (٧١,۶٥٪) و مولیبدن (٥٩,٢٧٪) بود. شاخص خطر غیرسرطان‌زایی برای کودکان برابر با ٢٠٠۴ به‌دست آمد که از حد ایمنی فراتر است و در این میان، واندیم زیست‌دسترس‌پذیر به‌عنوان عامل اصلی ریسک شناسایی شد. این یافته‌ها نشان می‌دهد که اتکای صرف بر غلظت کل عناصر بالقوه سمی می‌تواند گمراه‌کننده باشد و بر ضرورت انجام ارزیابی‌های مبتنی بر گونه‌پذیری شیمیایی برای توصیف دقیق رفتار زیست‌محیطی و مخاطرات سلامت ناشی از باطله‌های معدنی تأکید می‌کند.

نویسنده مسئول مکاتبات: *ahmed.abdelhameed@ejust.edu.eg* (الف.الف. عبدالحمید)